

Phase change and stress wave in picosecond laser–material interaction with shock wave formation

Chong Li · Jingchao Zhang · Xinwei Wang

Received: 4 March 2013 / Accepted: 8 May 2013 / Published online: 30 May 2013
© Springer-Verlag Berlin Heidelberg 2013

Abstract When background gas is present in pulsed laser–material interaction, a shock wave down to the nanoscale will emerge. The background gas will affect the phase change and explosion in the target. This study is focused on the void dynamics and stress wave in a model material (argon crystal) under picosecond pulsed laser irradiation. Our results show that existence of ambient gas and the shock wave significantly suppresses the void formation and their lifetime. Void dynamics, including their growing rate, lifetime, and size under the influence of ambient gas are studied in detail. All the voids undergo an accelerating and decelerating process in the growth. The collapsing process is almost symmetrical to the growing process. Higher laser fluence is found to induce an obvious foamy structure. Stress wave formation and propagation, temperature contour, and target and gas atom number densities are studied to reveal the underlying physical processes. Although the interaction of the plume with ambient gas significantly suppresses the void formation and phase explosion, no obvious effect is found on the stress wave within the target. Very interestingly, secondary stress waves resulting from re-deposition of ablated atoms and void collapse are observed, although their magnitude is much smaller than the directly laser-induced stress wave.

Keywords Laser–material interaction · Shock wave · Void dynamics · Stress wave

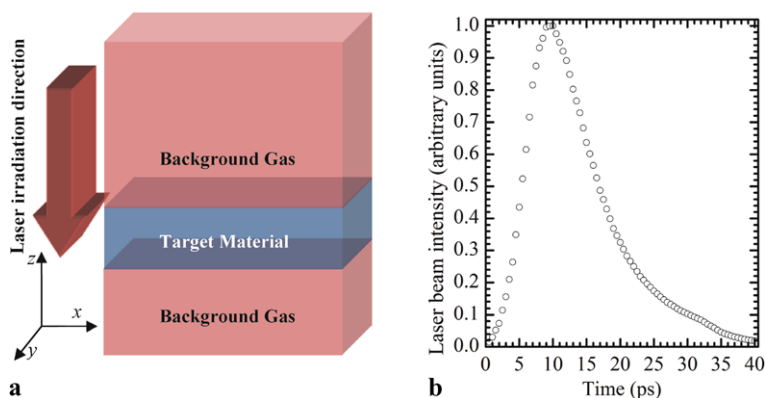
1 Introduction

Over the last few decades, interaction between material and ultra-fast pulsed lasers has captured significant attention because of the wide applications of ultra-fast lasers in matrix-assisted laser desorption/ionization (MALDI) [1], laser surgery, microfabrication, pulsed laser deposition (PLD) [2], etc. Laser–material interaction is an extremely complicated process involving optical absorption, mechanical stress generation and propagation, melting, vaporization, and solidification. When the incident laser energy is high enough for a specific material, phase explosion takes place. And, when laser–material interaction happens under an environment with ambient gas instead of vacuum, a shock wave could form. Numerous simulation and experimental studies have been carried out to investigate the above problems. Song and Xu [3] used nickel as the specimen to study the laser fluence threshold of phase explosion. In the molten region, nucleation and bubble growth during laser and material interaction have been experimentally explored by Park et al. [4] and Yavas et al. [5]. Experimental studies about plume structure, dynamics, and evolution have also been reported [6–8].

Accompanying the substantial experimental work, a large amount of simulation work at atomic level has been devoted to obtaining insight into the underlying physics of laser–material interaction. Molecular dynamics (MD) simulation, which analyzes the molecule/atom movement directly, has been widely applied to explore the material structure under laser irradiation and the processes and mechanisms of laser–material interaction [9]. Owing to the rapid development of computer technology, the number of atoms that can be studied in simulation has increased dramatically. In one outstanding work by Zhigilei et al. [10], the influence of laser irradiation parame-

C. Li · J. Zhang · X. Wang (✉)
Department of Mechanical Engineering, Iowa State University,
2010 Black Engineering Building, Ames, IA 50011, USA
e-mail: xwang3@iastate.edu
Fax: +1-515-2943261

Fig. 1 Illustration for domain construction and incident laser irradiation. **(a)** Blue region is the target and the red regions are the gas atoms. Laser irradiation is in the negative z direction. **(b)** Schematic of laser intensity distribution



ters like laser fluence, pulse duration, and initial temperature of the sample on laser ablation is studied systematically and dynamics of plumes is described in detail. Zhang and Wang explored the long-time material behavior in nanosecond laser–material interaction by using large-scale hybrid atomistic macroscale simulation [11]. Other simulation work of the ablation plume and ejected clusters, evaporation, and condensation can be found in the literature [10, 12–14].

The existence of background gas can significantly affect the dynamics evolution of gas environment, the ablated plume, and the specimen during laser ablation. Simulation about plume propagation in vacuum and background gas has been reported [14]. A nanoscale shock wave results from the interaction between ejected target atoms and ambient gas. Details of such shock wave behavior can be seen in Feng and Wang’s work [15] and visual evidence is provided by Porneala and Willis [16]. Gacek and Wang [17] gave a detailed description of the shock wave dynamics and evolution. Other phenomena related to the shock wave such as mutual mass penetration and a secondary shock wave have been explored by our laboratory [18, 19]. Voids and bubbles in the molten region are also great concerns of researchers since they are directly related to the phase-change process and final surface quality. Zhigilei et al. [10] systematically discussed the reason for nucleation and spallation. The tensile stress generated in laser ablation and the material’s ability to withstand the tensile stress are pointed out to be the key for material fracture.

Although laser–material interaction has been investigated widely, there still remain some interesting things not yet uncovered. This work studies void lifetime and the evolution process under the effect of ambient gas. Emphasis is placed on the investigation of physical parameters such as stress, temperature, and atom number density contour. Furthermore, the effect of ambient gas on stress wave generation and propagation in the solid is studied in detail.

2 Methodologies of simulation

Since argon has simple face-centered cubic (fcc) crystal structure and the interaction between atoms can be precisely and conveniently described by the Lennard–Jones (12-6) potential, it has been selected as the object to investigate laser ablation and the shock wave [9, 15, 17, 18]. In this work, for simplicity, we also choose argon as the crystal material to study and adopt a model similar to Gacek and Wang’s paper [17], as shown in Fig. 1a. A shock wave can only form when there exists an ambient gas around the crystal target which is going to be irradiated by a pulsed laser. Given that our purpose is to study the effect of background gas on other dynamics problems, and to save the computation cost, we choose argon as the ambient gas but at the same time we make some modifications to the Lennard–Jones potential to describe the interaction between gas atoms. The original Lennard–Jones (12-6) potential is expressed as

$$\phi_{ij} = 4\epsilon\left[\left(\frac{\sigma}{r_{ij}}\right)^{12} - \left(\frac{\sigma}{r_{ij}}\right)^6\right], \quad (1)$$

where the first term on the right represents the repulsive force potential and the second one is for the attractive force potential. We only consider the repulsive force in the interaction of gas–gas atoms and gas–target atoms, while we take both repulsive and attractive forces into account in the target–target atom interaction. ϵ and σ are well depth and equilibrium separation parameter of the LJ potential, which are set to 1.653×10^{-21} J and 3.406 Å, respectively. r_{ij} in the above equation denotes the pair separation that can be expressed as $r_{ij} = r_i - r_j$.

In this model, the argon lattice constant is 5.414 Å. The computation domain contains 337,500 atoms and measures $32.5 \times 2.7 \times 3627$ (nm³) ($x \times y \times z$). Figure 1b shows the incident laser beam intensity distribution with full width at half maximum (FWHM) of 11.5 ps peaked at 9 ps. In order to simulate the situation where the material exposed to a gas environment is irradiated by a laser pulse and eliminate the surface effect, we set the boundaries in the x , y , and z directions to be periodical. MD simulation work in

this article is performed with the LAMMPS package [20]. The equilibrium temperature chosen for this MD simulation is 50 K and the time step is set to 25 fs. The cutoff distance is chosen as 2.5σ . Before laser irradiation is applied, the whole system is thermostated and equilibrated at 50 K for 3.75 ns by running as a canonical (NVT) ensemble. After that, we run the whole system as a microcanonical (NVE) ensemble for 500 ps. When thermal equilibrium is reached, the pressure of the ambient gas is approximately 0.23 MPa. Because this work is to describe and study the phenomena related to the shock wave, there is no need to make the ambient gas pressure equal to 1 atm. Other specific details about the modeling can be found in Refs. [19, 21].

After equilibrium calculation, laser heating is applied on the target in the negative z direction and is absorbed volumetrically in the target. To realize energy absorption in space, the target is divided into a group of bins with equal thickness. For each time step, the incident laser energy is absorbed exponentially and can be expressed as [17]

$$\Delta E = E_0[1 - \exp(\delta z/\tau_0)], \quad (2)$$

where τ_0 is the adjusted real optical absorption depth and calculated as $\tau_0 = \tau\rho_0/\rho_1$. ρ_0 and ρ_1 are the densities of bin and whole target, respectively. τ is an artificial absorption depth. To add the absorbed energy into atoms within each bin, we scale the velocities of the atoms by a factor of [17]

$$\chi = \left\{ 1 + \Delta E / \left[0.5 \sum_{i=1}^N m_i ((v_{i,1} - \bar{v}_1)^2 + (v_{i,2} - \bar{v}_2)^2 + (v_{i,3} - \bar{v}_3)^2) \right]^{\frac{1}{2}} \right\}, \quad (3)$$

where $v_{i,j}$ and v_j are the velocity of atom i and the average velocity of atoms in each target bin in the x , y , and z directions. The new velocity of atom i is calculated as

$$v'_{i,j} = (v_{i,j} - \bar{v}_j) \cdot \chi + \bar{v}_j. \quad (4)$$

The laser induces the generation and propagation of a stress wave. Once the stress wave reaches the target bottom, it will be reflected and become tensile stress propagating towards the irradiation surface. When the tensile stress exceeds what the material can support, fracture of the material will emerge. With further propagation, the stress wave can possibly reach the vapor–liquid zone and finally affect the shock wave and other related phenomenon. To get rid of the artifact from stress wave reflection in the target, a region of 10 Å along the z axis is built at the bottom of the target. An external force specified by Eq. (5) is added to the atoms in this region [11, 17, 22]:

$$F_t = -\frac{\rho \cdot v \cdot c \cdot A}{N}, \quad (5)$$

where ρ is the density of the designated bottom layer, v the atom average velocity at each time step in the layer, c the propagation speed of the stress wave, which is approximately 1333 m/s, and A denotes the area normal to the incident laser beam. N is the number of atoms within the bottom layer at each time step. Our work [11, 17] has proved the validity of this method. During our MD simulation, atomistic snapshots and the velocity plots are examined. No movement of the target is observed and the stress wave is not reflected by the bottom. This means that the procedure of adding force is effective in eliminating the undesired stress wave reflection at the back boundary.

3 Results and discussion

3.1 General picture of phase change under shock wave

The cases with a laser fluence of 3 J/m² and an ambient gas pressure of 0.23 MPa are chosen to describe phase change under the existence of the shock wave. Figure 2 shows the shock wave evolution. Figure 2a is for the case $E = 3$ J/m² and $\tau = 5$ nm, and Fig. 2b is for $E = 3$ J/m² and $\tau = 15$ nm. They are similar to some cases which Gacek and Wang used in their analysis [17]. The study in this work is focused on the phase change and stress wave, not the shock wave itself, which has been studied in detail in the work by Gacek and Wang. In Fig. 2a the incident laser beam causes material to evaporate violently because its energy intensity exceeds the material ablation threshold. Quickly after the laser pulse stops at $t = 40$ ps, thermal expansion is predominant and a large number of atoms escape from the target surface because of high pressure from intense phase explosion. The ejected plume moves at a speed higher than the sound velocity, and serves like a piston to compress the ambient gas and finally leads to the formation of an evidently strong shock wave at the nanoscale.

Comparison among the process at 2 ns, 3 ns, and 4 ns in Fig. 2a demonstrates that the plume is stopped from propagating forward and is slightly moving backward starting from 3 ns (as the blue arrows indicate in Fig. 2a).

The thermodynamic properties including density, temperature, pressure, and velocity of the shock wave front change dramatically during its propagation. At 0.5 ns in Fig. 2a, a dense red region is already distinguished, which represents the shock wave expansion front. The front of the shock wave has the highest density, and the density becomes smaller towards the plume–gas interface. The velocity, temperature, and pressure show the same trend as density. Detailed analysis can be seen in our previous work [15, 17, 18]. This work will present these parameters with contours in a longer time scale within the whole simulation space to give a more in-depth analysis in the following part.

The laser absorption depth can be varied to control the energy distribution in the target. When the absorption depth

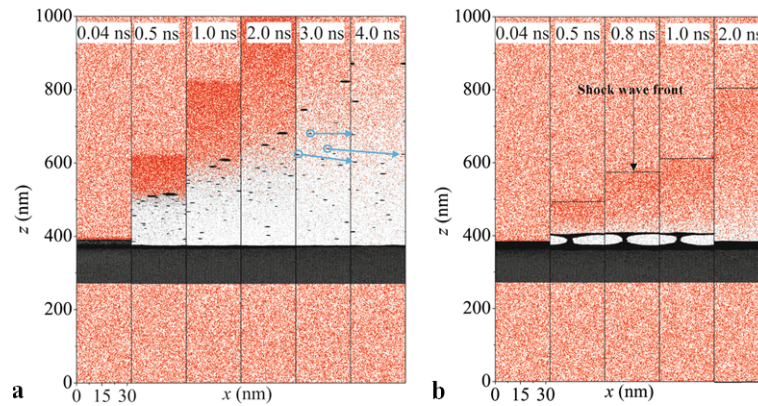


Fig. 2 Snapshots for shock wave formation and dynamics evolution. (a) Incident laser fluence $E = 3 \text{ J/m}^2$ and the absorption depth τ is 5 nm; (b) $E = 3 \text{ J/m}^2$ and $\tau = 15 \text{ nm}$. Red dots in the atomistic snapshots represent the gas atoms while black ones are for target atoms. Dense red region is the shock wave front, as shown by the dotted line

is increased from 5 nm to 15 nm, the phenomenon of phase change under the shock wave is dramatically different from that before. Details are shown in Fig. 2b. There is still a plume generated from laser ablation. However, because fewer atoms are ejected, the plume is much less visible as shown by the comparison between (a) and (b) in Fig. 2. The dark red region that represents the shock wave is barely distinguished in Fig. 2b. It is found that at $t = 0.5 \text{ ns}$, the shock wave front velocity decreases from 550 m/s at $\tau = 5 \text{ nm}$ to 290 m/s at $\tau = 15 \text{ nm}$, although it is still larger than the local sound speed of 132 m/s in the ambient gas. Because of the low energy gained by the shock wave for $\tau = 15 \text{ nm}$, the plume and the dark red region will dissipate soon in the ambient gas. Interestingly, when the laser absorption length is set to 15 nm, a large void is observed during the time 0.5–1.0 ns. The dynamics of void evolution in the molten region will be discussed in detail in the next subsection.

3.2 Phase change and void dynamics in molten region

Essentially, voids are fractures or spallation in a material during laser–material interaction. Figure 3 depicts the void evolution. Figure 3a is for the case $E = 3 \text{ J/m}^2$, $\tau = 15 \text{ nm}$, with ambient gas; Fig. 3b is for the case $E = 2.5 \text{ J/m}^2$, $\tau = 15 \text{ nm}$, ambient gas is included in this model; and Fig. 3c for the case $E = 3 \text{ J/m}^2$, $\tau = 15 \text{ nm}$, without ambient gas. As illustrated in Fig. 3b, at the end of laser irradiation (0.04 ns), voids are hardly visible. Only the solid and molten regions can be distinguished. However, when it comes to 0.10 ns, 60 ps after the laser irradiation, several voids are observed. They nucleate and grow, and then collapse soon.

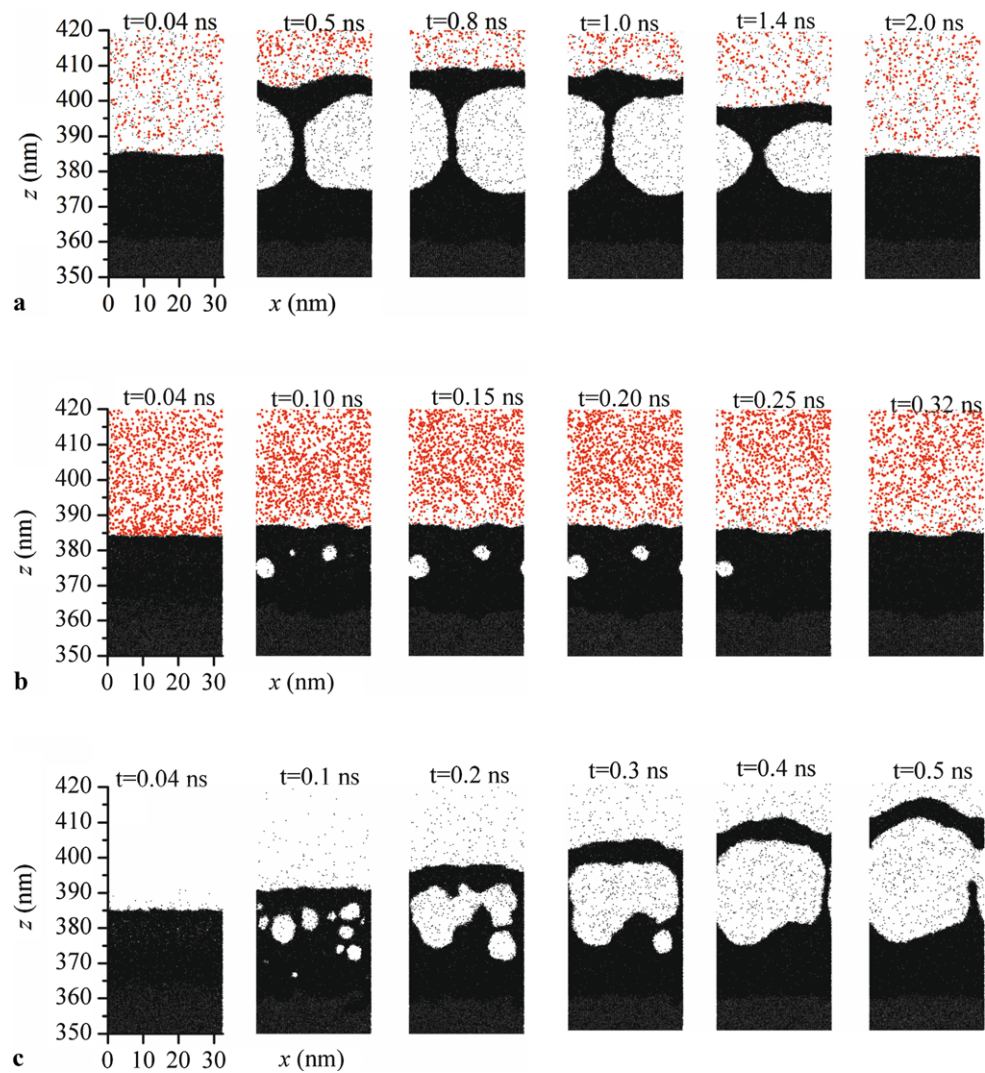
Both temperature and tensile stress play important roles in void formation. When $E = 3 \text{ J/m}^2$, $\tau = 15 \text{ nm}$, at the

in the figures. The shock wave is less visible for $\tau = 15 \text{ nm}$ than for $\tau = 5 \text{ nm}$. A big void exists in (b) from 0.5 ns to 1.0 ns. Blue arrows mark the movement of three specific clusters. Slight backward movement is observed from 3 ns to 4 ns

end of laser irradiation, the target surface reaches the thermodynamic critical temperature $T_{tc} = 150.87 \text{ K}$ for argon, while, for $E = 2.5 \text{ J/m}^2$, $\tau = 15 \text{ nm}$, the highest temperature is around 60 K. Comparison of these two cases at the beginning of nucleation reveals that nucleation will increase dramatically around the critical point, which is supported by the conclusion for superheating under a short laser pulse with a high fluence [23]. Phase explosion during overheating is constrained by the ambient gas as the difference shown in Figs. 3a and 3c. Zhigilei and Garrison [24] pointed out that the tensile stress resulting from the interaction of laser-induced pressure with the free surface is the mechanical reason for void formation. It takes time for the tensile stress to propagate along the irradiation direction and reach a certain depth, where the maximum tensile strength exceeds the material's limit and consequently void formation is observed. In addition, the ability of a material to support tensile stresses depends on temperature [10]. The tensile strength limit of a material decreases as the temperature approaches the melting point. Figure 7 shows the atomic snapshots and stress wave for the case $E = 3 \text{ J/m}^2$, $\tau = 15 \text{ nm}$. Clearly, the tensile stress does not attain the maximum value at $z = 375 \text{ nm}$. However, voids are observed around $z = 375 \text{ nm}$ in Fig. 3a. The relationship between the tensile stress limit and temperature should account for this phenomenon.

In this work, comparison between void evolution under laser fluences of 3 J/m^2 and 2.5 J/m^2 is conducted. We can see that from the comparison between Figs. 3a and 3b, when the laser energy is increased, at the beginning of void formation, a wider molten region and a violent foamy structure are observed. With more energy absorbed during laser irradiation, more atoms gain enough energy to overcome the constraint force from the ambient gas and other solid atoms. At 0.5 ns, a large void is observed around $z = 370 \text{ nm}$ when $E = 3 \text{ J/m}^2$ while in Fig. 3b the voids have collapsed. It can

Fig. 3 Snapshots of void evolution: (a) $E = 3 \text{ J/m}^2$ and $\tau = 15 \text{ nm}$ with ambient gas. (b) $E = 2.5 \text{ J/m}^2$ and $\tau = 15 \text{ nm}$ with ambient gas. During 0.04–0.32 ns, void formation, growth, and collapsing process is demonstrated. (c) $E = 3 \text{ J/m}^2$ and $\tau = 15 \text{ nm}$ without ambient gas. In order to have a close view of the void dynamics, only atoms within the 350–420 nm range in the z direction are plotted



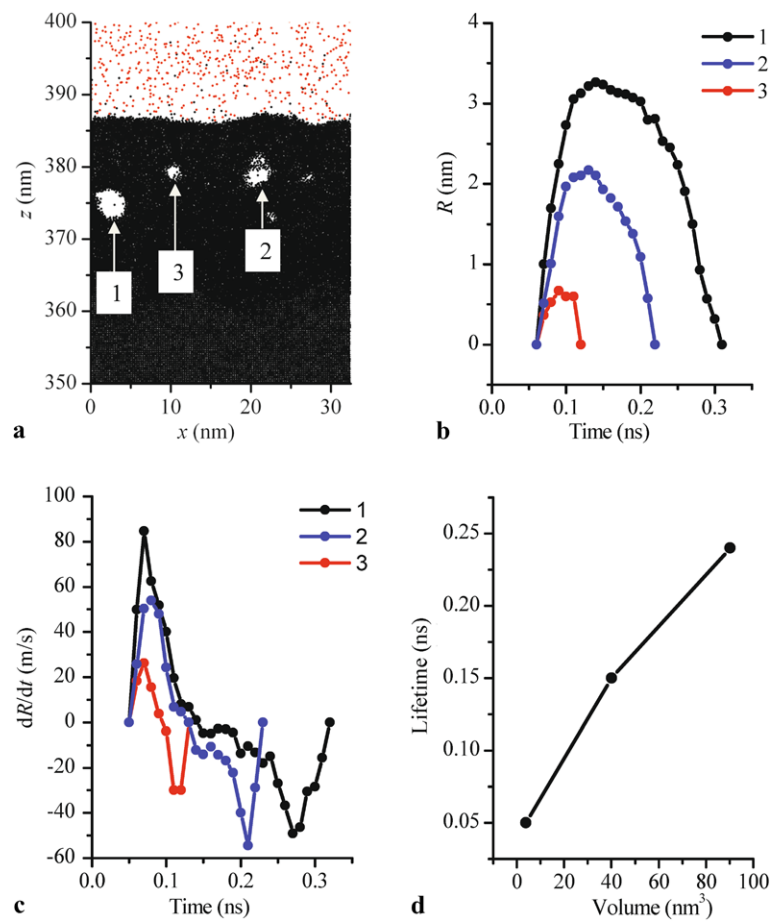
be noted from Fig. 3b that there are still some voids forming and then collapsing. In this situation, the recoil effect from the ejected cluster and plume can also prevent some of the voids from growing and forces them to collapse significantly. In Fig. 3a all the voids form and grow into a big-size void and then gradually collapse. The existence of background gas does affect the phase change and void dynamics. When the ambient gas is considered at the laser fluence of 3 J/m^2 , a collapse process is observed. However, for the scenario without ambient gas, a layer of atoms with a thickness of 10 nm in the z direction flies out.

Figure 4 shows the void evolution process and their lifetime under the situation of $E = 2.5 \text{ J/m}^2$, $\tau = 15 \text{ nm}$ with the target placed in the gas environment. Figure 4a illustrates the index of voids studied in this figure. From the two-dimensional (2D) view it is noted that the voids are not exactly circular. Therefore, an effective radius is used to describe the volume change. First of all, the 2D area of the voids is evaluated by MATLAB Image Processing Toolbox.

Then the effective radius is derived by calculating the radius of a circle with the corresponding equal area. Finally, the effective volume can be obtained by multiplying the effective area by the length in the y direction (thickness), namely 2.7 nm. Figure 4b shows the radius change and the derivative of radius against time is calculated to describe the void growing/collapsing speed, as shown in Fig. 4c. Based on Fig. 4c, the lifetime of voids can be calculated and is shown in Fig. 4d.

We can see that void 1, which is located at the left-hand side, has the biggest volume and longest lifetime while void 3, the one at $x = 10 \text{ nm}$, has the shortest lifetime. All the voids experience a volume increase and decrease process during their lifetime. For void 1, it starts to grow with a relatively small rate at 0.04 ns and then reaches the maximum growth rate of 85 m/s. Subsequently, it will grow with a smaller rate until reaching the maximum volume at 0.11 ns. After that it begins to contract and collapse. For voids with a large volume, there is a period within which the void

Fig. 4 Void dynamics for $E = 2.5 \text{ J/m}^2$, $\tau = 15 \text{ nm}$: (a) void identity, snapshot for $t = 0.08 \text{ ns}$ is chosen for identity definition; (b) void radius at different times; (c) void radius evolution rate; (d) relationship between void lifetime and void volume



is quite stable. Void 1 is approximately stable from 0.12 ns to 0.18 ns (Fig. 4c). Interestingly, from this figure we also notice that the growth and collapse processes are almost symmetric. Under the effect of tensile stress, the voids at first grow up quickly. However, the attraction force from the molten region and the repulsive force from ambient gas work together to prevent the voids from expansion. When the effect of the restraint force is dominant, we see a decelerating growth process. Otherwise, the voids will grow with an increasing rate. Generally, voids with a larger volume have a larger maximum growth rate of about 85 m/s, just like void 1. For smaller voids, such as void 3, it has a much smaller peak change rate, approximately 26 m/s. The model used in our work is a quasi-three-dimensional model considering it is relatively thin in the y direction. The shape of the voids is cylindrical rather than spherical. Thus, the evolution may be affected by the size constraint in the y direction.

3.3 Dynamic physical process under the effect of shock wave

Comparison of temperature, stress, and target atom number and gas atom number densities is made in this work for detailed physical process analysis. Figure 5 depicts the spa-

tiotemporal temperature and stress contours for $E = 3 \text{ J/m}^2$, $\tau = 5 \text{ nm}$ and $E = 3 \text{ J/m}^2$, $\tau = 15 \text{ nm}$, respectively. The slope line represents the movement of the shock wave. There is a temperature rise in the place where the shock wave travels. The ambient gas significantly reduces the velocity of the expansion plume and the speed of the leading shock wave front decreases from 550 m/s at 0.5 ns to 360 m/s at 3 ns for $E = 3 \text{ J/m}^2$ and $\tau = 5 \text{ nm}$. The curved temperature profile in Figs. 5a and 5b also indicates this speed decrease. Figure 6 shows the atom number density contours for target and gas corresponding to these two cases. The time starts from the beginning of the laser irradiation and lasts for almost 5 ns in the simulation. For the target atom number density contour, there are dark and light strips which indicate the inequality of atom number density (Figs. 6c and 6d). However, this is a false impression. To get the number density contour, the whole simulation box has to be divided into a number of small bins. In this work, for the contours, including the target atom and gas atom number density contours and stress contours, the whole space is divided into bins of 1 nm thickness in the z direction. Since the lattice constant of argon crystal is 5.414 \AA , 10 \AA is definitely not a multiple of that. So, the atoms contained in the bins may fluctuate in number slightly. This explains the dark and light strip lines in our

Fig. 5 (a) Spatiotemporal temperature contour for $E = 3 \text{ J/m}^2$, $\tau = 15 \text{ nm}$; (b) temperature contour for $E = 3 \text{ J/m}^2$, $\tau = 5 \text{ nm}$, zoom-in plot is used to illustrate the temperature relationship with stress wave; (c) stress contour for $E = 3 \text{ J/m}^2$, $\tau = 15 \text{ nm}$; (d) stress contour for $E = 3 \text{ J/m}^2$, $\tau = 5 \text{ nm}$. The slope lines in the temperature contours indicate the development of the shock wave. There is a temperature drop along time in the contours. A secondary stress wave is shown in (c) in the zoom-in figure

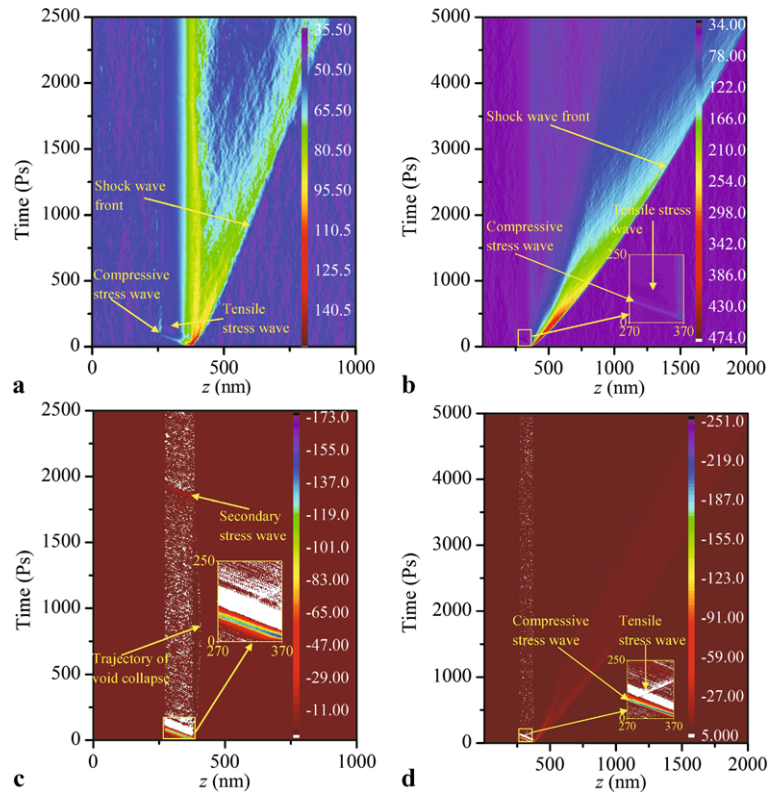
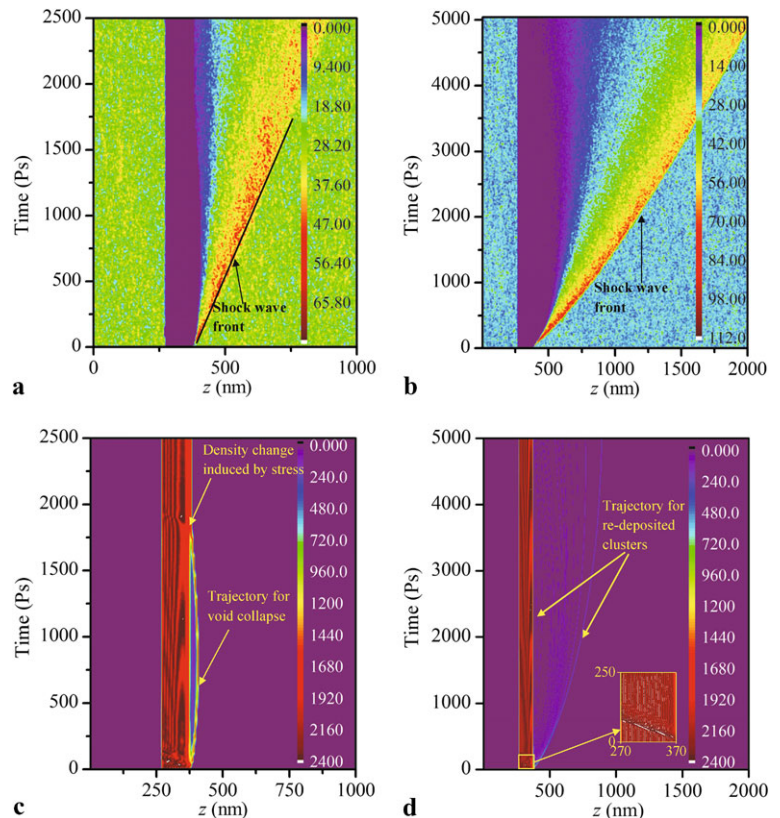


Fig. 6 Atom number density contour: (a) gas number density contour for $E = 3 \text{ J/m}^2$, $\tau = 15 \text{ nm}$; (b) gas number density contour for $E = 3 \text{ J/m}^2$, $\tau = 5 \text{ nm}$; (c) target number density contour, $E = 3 \text{ J/m}^2$, $\tau = 15 \text{ nm}$; (d) target number density contour, $E = 3 \text{ J/m}^2$, $\tau = 5 \text{ nm}$. Stress waves can be seen from the deformed twisted lines in the number density contours, indicating that the local density is changed by the local stress wave. Void collapse in (c) leads to a secondary stress wave



contours, especially for the target part. For the temperature contour, an interval of 21.656 \AA is used in the z direction.

The absorption depth does strongly impact phase change and stress wave evolution. The increase of absorption depth can expand the depth of receiving a significant amount of laser energy. The shock wave expansion velocity is different for the two absorption depths used here. For 3 J/m^2 , $\tau = 5 \text{ nm}$, the shock wave moves faster. As shown in Fig. 5a, at 2.5 ns , the shock wave generated by the laser irradiation of 3 J/m^2 , $\tau = 5 \text{ nm}$ moves to the vicinity of $z = 1300 \text{ nm}$, while the one induced by laser irradiation of 3 J/m^2 , $\tau = 15 \text{ nm}$ only travels to a place right below $z = 1000 \text{ nm}$ (shown in Fig. 5b).

At the beginning, the ejected clusters characterize the maximum temperature. With the time going by, the temperature will go down because of the interaction of target atoms with gas. In the corresponding part of the temperature contour, along the oblique line the temperature drops gradually, as shown in Figs. 5a and 5b. Part of the plume's translational kinetic energy is converted into its thermal energy. The temperature will go down with the increase of absorption depth. For $E = 3 \text{ J/m}^2$, $\tau = 5 \text{ nm}$, the maximum temperature is 476 K , while, with the same laser fluence and $\tau = 15 \text{ nm}$, the temperature of the target only goes to 154 K . The maximum temperature occurs near the end of laser irradiation.

Re-deposition is different for the two cases. For $E = 3 \text{ J/m}^2$, $\tau = 15 \text{ nm}$, a large part of the target atoms is pushed out while at around 1.8 ns this part re-combines with the rest of the target (Fig. 5c). By contrast, with a shorter absorption depth, 5 nm , Fig. 5d shows that some of the target atoms are removed from the upper surface. The curves in Figs. 5d and 6d demonstrate the trajectories of the ejected atoms. From Fig. 6d we can observe that some of the ablated atoms/clusters already re-combine with the target within the 5 ns time while some of them will take a longer time to come back. Clusters flying out will decompose with time and slow down and finally re-deposit on the surface. When the atoms/clusters re-combine with the target, they will strike the target and could cause a strong secondary stress wave in the target. Such phenomenon will be discussed in detail in the next subsection.

3.4 Stress wave in the target with shock wave formation

Multiple stress waves are observed in our MD study. The laser-induced stress wave consists of a strong compressive component and a weak tensile component. The interaction of the compressive stress wave with the interface and the relief of compressive stress may account for the generation of the tensile component. A similar phenomenon and a detailed explanation can be seen in Wang's work [25] and Wang and Xu's work [26]. The stress wave during laser-material interaction has already been investigated intensively. The effects

of laser irradiation duration on the induced stress wave and the relationship between compressive stress, tensile stress, and the laser fluence have been discussed before [10]. In this work, the difference of the stress between situations with and without ambient gas is explored in detail.

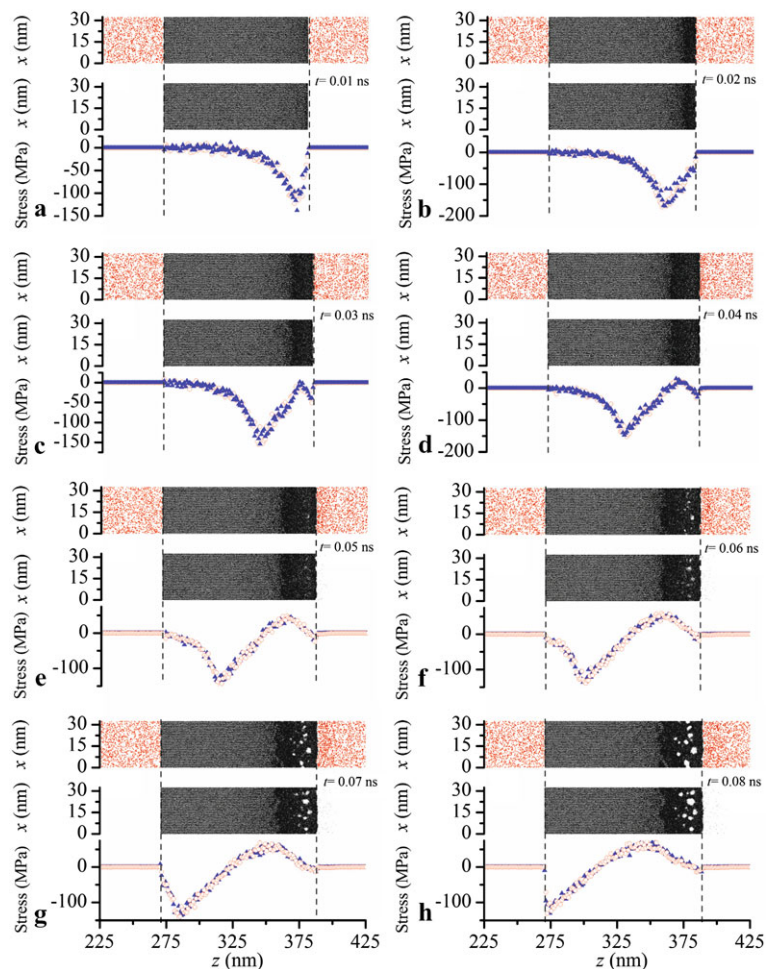
The existence of gas does play a role in the phase change. However, as to the generation and propagation of the stress wave, no big difference is distinguished. Stress is a main driving force behind the fracture formation during laser ablation. As to the generation of the stress wave, it is believed to result from the direct laser energy absorption as well as the recoil driving force from target atom ejection [10]. Figures 7 and 8 show the stress wave generation and propagation for $E = 3 \text{ J/m}^2$, $\tau = 5 \text{ nm}$ and $\tau = 15 \text{ nm}$. The existence of ambient gas hampers the excited target atoms from expanding in the space and there are differences in the development of the molten regions. However, in all the plots of the two figures, no deviation is observed for stress with and without ambient gas. The momentum of the plume is significantly larger than the restraint force from the ambient gas. So, the stress wave shows no big difference in the solid.

Noticeably, from target atom number density (Figs. 6c and 6d) and temperature contours (Figs. 5a and 5b), the stress wave within the target can also be seen. Deformed fold lines in the target number density contours show the change of target density due to the local stress. Additionally, as marked in Fig. 5a, the stress wave can also be detected by the change of temperature. The tensile stress will come along with a temperature decrease while compressive stress induces a temperature increase.

The reasons for the stress wave generation vary from each other. Laser-induced compressive stress appears first and then it is the tensile stress wave (Fig. 5d). The compressive and tensile components always accompany each other. The stress waves are not entirely gone at the bottom of the target. However, for the residual stress, the magnitude is very small and even negligible. Another relatively large stress wave is caused by void collapse or cluster re-deposition. Here we name it the secondary stress wave. In Fig. 5c, the trajectory of collapse is marked. In Figs. 5c and 6c the upper layer atoms are dragged back at 1.8 ns . Right after this we can see the stress wave in the stress contour or atom number density contour. The magnitude of this kind of secondary stress wave is much less than the stress wave directly induced by laser irradiation. For $\tau = 15 \text{ nm}$, the maximum stress value is approximately -140 MPa . In contrast, the maximum value of the secondary stress wave is only about -15 MPa . The trajectory of the re-deposited cluster is marked in Fig. 6d. Similarly, the induced second stress wave is very small in magnitude.

We can see from the stress evolution figures (Figs. 7 and 8) that when the absorption depth is 5 nm rather than 15 nm , there is a sharp drop in the stress wave front. That energy absorption is focused on the upper layer for the ab-

Fig. 7 Phase change and stress wave for $E = 3 \text{ J/m}^2$, $\tau = 15 \text{ nm}$. Two cases with and without ambient gas are compared here. The *blue symbol* is for the case without ambient gas and the *red one* is for the case with ambient gas. The negative stress peak is the maximum value of the compressive stress and the positive peak is for maximum tensile stress. No obvious difference for the stress wave is observed between gas and non-gas situations. To help identify the relative position of the stress wave in the physical domain, the atomic configurations are also plotted. The *red dots* are for gas atoms and the *black dots* are for target atoms



sorption depth of 5 nm and accounts for this phenomenon. Interestingly, In Fig. 8, there is one more peak compared to Fig. 7, which represents pressure in the flying-out part. This part has been marked in Fig. 8c for $t = 0.03 \text{ ns}$. As the time is going by, the peak is moving along the positive z direction.

Figure 9 shows the relationship between the magnitude of the stress wave at 0.04 ns versus the laser energy. With the increase of the laser fluence, the magnitude of the stress increases dramatically (almost linearly) (Fig. 9b). In Fig. 9a all the laser energy is absorbed under the same absorption length $\tau = 15 \text{ nm}$. Three peaks are identified in the figure. From the right-hand side, the first one represents the ejected clusters while the second and third ones are the tensile and compressive components within the target. A sharp drop is observed in the stress wave front for the stress wave propagation for larger laser fluences and the ejected clusters move faster with the rise of the laser energy.

4 Conclusions

In this work, systematic atomistic modeling has been conducted to study the shock wave formation in picosecond

laser–material interaction and phase change and stress wave development and propagation with the existence of the shock wave. The voids grew at a fast speed and then decelerated in growth. Larger voids were found to maintain their large volume for a longer time. As to the contraction and collapsing process, all the voids experience fast contracting and then disappear slowly, and this process is almost symmetrical to the growing process with respect to time. Background gas significantly suppressed the void growth and their lifetime. No effect from the ambient gas on the stress wave in the solid was observed in this work. The decrease of the absorption depth and the increase in laser fluence led to a sharp drop in the stress wave front. Furthermore, ablated cluster re-deposition and void collapse were found to generate a secondary stress wave in the target. The magnitude of this secondary ($\sim 15 \text{ MPa}$) stress wave is much smaller than that of the first primary laser-induced stress wave ($\sim 140 \text{ MPa}$). There is a close, almost linear relationship between the laser fluence and the stress wave maximum value. Under a laser fluence of 40 J/m^2 , the stress wave in the target has a maximum compressive component exceeding 1.5 GPa.

Fig. 8 Phase change and the stress wave generation and propagation for $E = 3 \text{ J/m}^2$, $\tau = 5 \text{ nm}$. Two cases with and without ambient gas are compared here. The *blue symbol* is for the case without ambient gas and the *red one* is for the case with ambient gas. A sharp drop is observed in the stress wave front. This is the big difference induced by the absorption depth of $\tau = 5 \text{ nm}$ to $\tau = 15 \text{ nm}$. To help identify the relative position of the stress wave in the physical domain, the atomic configurations are also plotted. The *red dots* are for gas atoms and the *black dots* are for target atoms

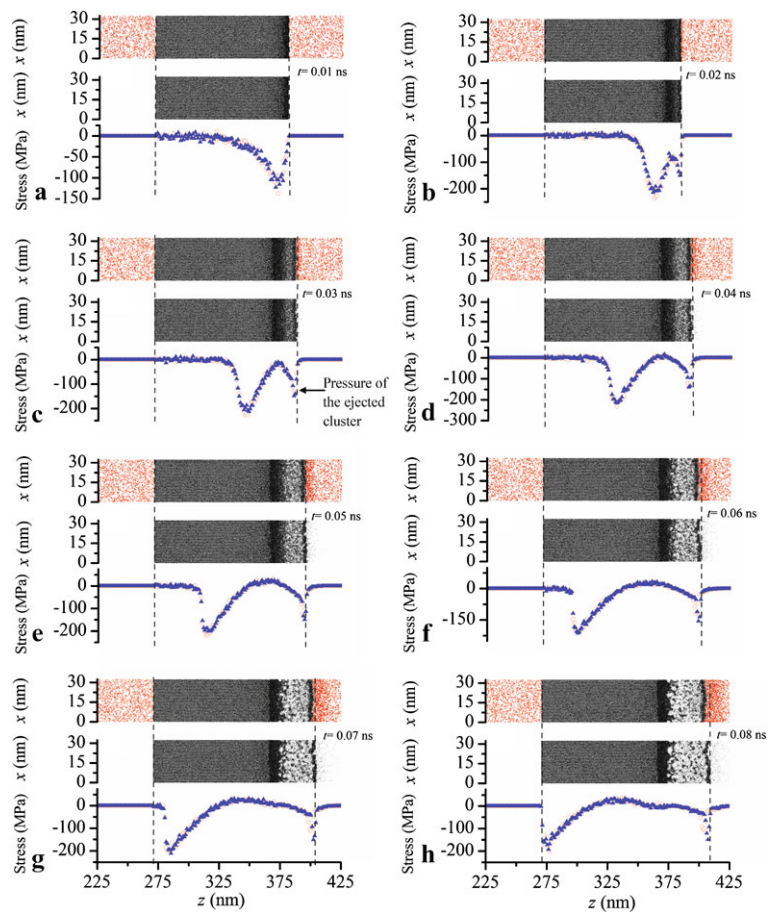
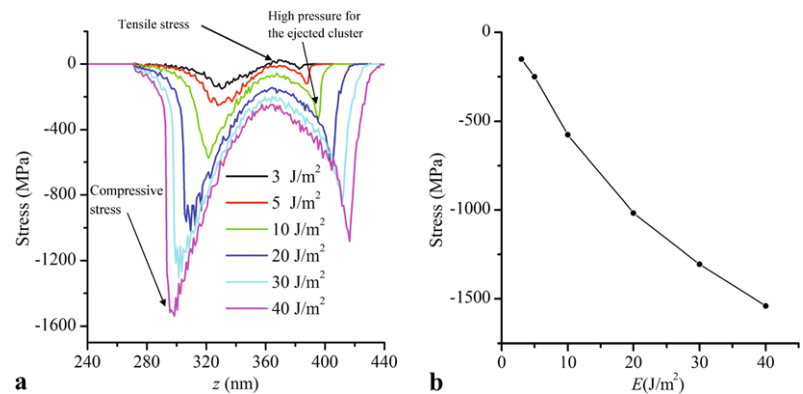


Fig. 9 Comparison of stress waves for different laser fluences: (a) the stress wave in the target at $t = 0.04 \text{ ns}$ and (b) the relationship between the stress wave maximum value and the laser fluence. All the cases are run under the same gas environment



Acknowledgements Support of this work by the National Science Foundation (No. CMMI-1029072) is gratefully acknowledged. X.W. thanks the great support of the ‘Taishan Foreign Scholar’ program of Shandong Province, China.

References

- P. Seng, M. Drancourt, F. Gouriet, B. La Scola, P.E. Fournier, J.M. Rolain, D. Raoult, Clin. Infect. Dis. **49**, 543 (2009)
- M.N.R. Ashfold, F. Claeysens, G.M. Fuge, S.J. Henley, Chem. Soc. Rev. **33**, 23 (2004)
- K.H. Song, X.F. Xu, Appl. Surf. Sci. **127**, 111 (1998)
- H.K. Park, C.P. Grigoropoulos, C.C. Poon, A.C. Tam, Appl. Phys. Lett. **68**, 596 (1996)
- O. Yavas, P. Leiderer, H.K. Park, C.P. Grigoropoulos, C.C. Poon, W.P. Leung, N. Do, A.C. Tam, Appl. Phys. A **58**, 407 (1994)
- S.S. Harilal, C.V. Bindhu, M.S. Tillack, F. Najmabadi, A.C. Gaeris, J. Appl. Phys. **93**, 2380 (2003)
- D.B. Geohegan, Thin Solid Films **220**, 138 (1992)
- S. Amoroso, R. Bruzzese, M. Vitiello, N.N. Nedialkov, P.A. Atanasov, J. Appl. Phys. **98**, 044907 (2005)
- X.W. Wang, X.F. Xu, J. Heat Transf. **124**, 265 (2002)
- L.V. Zhigilei, E. Leveugle, B.J. Garrison, Y.G. Yingling, M.I. Zeifman, Chem. Rev. **103**, 321 (2003)
- L. Zhang, X. Wang, Appl. Surf. Sci. **255**, 3097 (2008)
- L.V. Zhigilei, B.J. Garrison, Appl. Phys. Lett. **71**, 551 (1997)

13. L.V. Zhigilei, *Appl. Phys. A* **76**, 339 (2003)
14. J.N. Leboeuf, K.R. Chen, J.M. Donato, D.B. Geohegan, C.L. Liu, A.A. Puretzky, R.F. Wood, *Phys. Plasmas* **3**, 2203 (1996)
15. X. Feng, X. Wang, *Phys. Lett. A* **369**, 323 (2007)
16. C. Porneala, D.A. Willis, *Appl. Phys. Lett.* **89**, 211121 (2006)
17. S. Gacek, X. Wang, *Appl. Phys. A* **94**, 675 (2009)
18. L. Zhang, X. Wang, *Jpn. J. Appl. Phys.* **47**, 964 (2008)
19. S. Gacek, X. Wang, *J. Appl. Phys.* **104**, 126101 (2008)
20. S. Plimpton, *J. Comput. Phys.* **117**, 1 (1995)
21. X. Wang, *J. Phys. D, Appl. Phys.* **38**, 1805 (2005)
22. L.V. Zhigilei, B.J. Garrison, *Mater. Res. Soc. Symp. Proc.* **538**, 491 (1999)
23. A. Miotello, R. Kelly, *Appl. Phys. Lett.* **67**, 3535 (1995)
24. L.V. Zhigilei, B.J. Garrison, *J. Appl. Phys.* **88**, 1281 (2000)
25. X. Wang, *J. Heat Transf.* **126**, 355 (2004)
26. X. Wang, X. Xu, *Int. J. Heat Mass Transf.* **46**, 45 (2003)